

## ORIGINAL RESEARCH ARTICLE

# Predicting effective thermal conductivity of sintered nano-Ag with artificial neural networks

Libo Zhao<sup>1†</sup>, Jiahui Wei<sup>1†</sup>, Yanwei Dai<sup>1\*</sup>, Daowei Wu<sup>2</sup>, Yuting Zhang<sup>2</sup>,  
 Kui Li<sup>3</sup>, and Fei Qin<sup>1</sup>

<sup>1</sup>Department of Mechanics, Institute of Electronics Packaging Technology and Reliability, Beijing University of Technology, Beijing, China

<sup>2</sup>Advanced Packaging Division, Xi'an Institute of Microelectronics Technology, Xi'an, Shaanxi, China

<sup>3</sup>R&d Innovation Center, Xi'an Institute of Microelectronics Technology, Xi'an, Shaanxi, China

(This article belongs to the *Special Issue: AI for Multiscale Analysis and Defect Identification in Packaging Structures and Semiconductor Chips*)

## Abstract

Due to the demand for high reliability and thermal conductivity of high-power modules operating at high temperatures, sintered nano-silver (Ag) has garnered significant attention as an excellent interconnect and heat transfer layer, particularly for its thermal conductivity and other reliability research. Since the mechanical behavior and heat conduction capacity of sintered Ag is generally regulated by changes in temperature, its microstructure will change accordingly, affecting its performance. In this study, a machine learning model was used to evaluate and predict the thermal conductivity of sintered Ag, providing an effective method to analyze the influence of microstructural characteristics on its heat transfer properties. Image processing and model simulation of scanning electron microscopy images of sintered nano-Ag nanostructures were performed using MATLAB and Ansys software. A batch calculation of the thermal conductivity of 2D images of sintered nano-Ag nanostructures was performed to obtain sufficient data sets. Based on the artificial neural network model of Bayesian optimization, the equivalent thermal conductivity of different sintered nano-Ag microstructures was predicted with high accuracy using the microstructure image and characteristic parameters of sintered nano-Ag. The proposed method enables rapid, effective, and accurate evaluation and prediction of the thermal conductivity of sintered nano-Ag, contributing significantly to the reliability of power modules.

**Keywords:** Artificial neural networks; Sintered nano-Ag; Effective thermal conductivity; Finite element modeling

*†These authors contributed equally to this paper.*

**\*Corresponding author:**

Yanwei Dai  
 (ywdai@bjut.edu.cn)

**Citation:** Zhao L, Wei J, Dai Y, *et al.* Predicting effective thermal conductivity of sintered nano-Ag with artificial neural networks. *Int J AI Mater Design*. 2025;2(1):8-20. doi: 10.36922/ijamd.5744

**Received:** November 1, 2024

**1st revised:** December 10, 2024

**2nd revised:** December 19, 2024

**3rd revised:** January 13, 2025

**Accepted:** January 15, 2025

**Published online:** February 6, 2025

**Copyright:** © 2025 Author(s). This is an Open-Access article distributed under the terms of the Creative Commons Attribution License, permitting distribution, and reproduction in any medium, provided the original work is properly cited.

**Publisher's Note:** AccScience Publishing remains neutral with regard to jurisdictional claims in published maps and institutional affiliations.

## 1. Introduction

Silicon carbide (SiC)-based power devices face limitations in achieving more effective energy conversion. To address the high reliability and thermal conduction demands of power modules operating at high temperatures, sintered nano-silver (Ag) has been developed and utilized frequently as the die-attaching material for SiC devices, due to its excellent performance in heat transfer and chip joining.

However, the mechanical behavior and heat conduction ability of sintered nano-Ag generally vary under different power cycling conditions, possibly due to damage accumulation and crack formation within its structure.<sup>1</sup> These variations in thermal performance could reduce the reliability of the modules and even lead to their failure. Thus, accurate evaluation and prediction of heat conductivity of sintered nano-Ag are essential.

To calibrate the effective thermal conductivity of sintered nano-Ag, different methods have been presented to understand the variations of effective thermal conductivity. Ordóñez-Miranda *et al.*<sup>2</sup> measured and calculated the thermal conductivity of sintered nano-Ag for a sample with 22% porosity, demonstrating that pancake-shaped pores have a more prominent effect on thermal conductivity compared to sphere pores through numerical comparisons. Signor *et al.*<sup>3</sup> computed the thermal conductivity of sintered nano-Ag with finite element analysis using actual 3D microstructures. Recently, Sghuri *et al.*<sup>4</sup> tested the thermal conductivity of sintered nano-Ag under aging conditions to obtain the thermal conductivity of sintered nano-Ag more directly. Meanwhile, Hu *et al.*<sup>5</sup> explored the process-microstructure-thermal relation using focused ion beam scanning electron microscopy. Although these studies have reported various behavior of sintered nano-Ag, predicting its thermal conductivity remains a major challenge due to the complexity of the process and flaw-dependent thermal behavior.

Various analytical and numerical methods have been developed to predict the effective thermal conductivity of sintered nano-Ag. Zhao *et al.*<sup>6</sup> indicated that the existing models are not suitable for predicting the thermal conductivity of sintered nano-Ag due to its high porosity and complex microstructure. Qin *et al.*<sup>7</sup> have presented a semi-analytical formulation to predict the effective thermal conductivity of sintered nano-Ag by considering the modification in the microstructure. To investigate changes in the effective thermal conductivity of sintered nano-Ag due to crack formation, they also proposed a semi-analytical formulation to predict the effect of cracks on the heat conductivity of sintered nano-Ag.<sup>8</sup> Lately, the effect of mud cracking on the heat conductivity of sintered nano-Ag was also studied,<sup>9</sup> revealing variations in heat transfer behaviors of sintered nano-Ag in the entire SiC module. Kim *et al.*<sup>10</sup> also studied the effect of pore shape and porosity on the effective thermal conductivity of sintered nano-Ag.

With the development of artificial intelligence, the prediction of thermal conductivity for different materials with machine learning methods has garnered significant attention due to advantages, such as high accuracy, efficiency, and potential for physics-based interpretation.<sup>11-16</sup> Predicting mechanical and material properties using

machine learning-assisted methods has also garnered significant attention in electronic packaging. Machine learning has been applied to different aspects of electronic packaging, such as materials extraction,<sup>17-19</sup> solder fatigue lifetime prediction,<sup>20-22</sup> defect detection,<sup>23</sup> and mechanical response prediction.<sup>24</sup> In the field of electronic packaging, Long *et al.*<sup>25</sup> proposed a convolution neural network (CNN)-assisted nanoindentation method to rapidly determine the mechanical properties of thin-film elastoplastic materials and predict the constitutive parameters with high accuracy. Recently, Du and coworkers<sup>26,27</sup> adopted CNN for support vector regression models to predict the thermal conductivity of sintered nano-Ag, demonstrating the potential applications of machine learning in predicting the thermal conductivity of sintered nano-Ag. However, machine learning requires large datasets. In addition, neural networks have demonstrated great potential in predicting the mechanical and thermal behavior of porous materials. For example, Wei *et al.*<sup>28</sup> used three different machine learning approaches to quickly and accurately predict the equivalent thermal conductivity of composite materials. Similar studies have been conducted in recent years.<sup>18,29,30</sup>

In this study, we focus on the research status and existing problems of physical and mechanical parameter evaluation methods for sintered nano-Ag nanomaterials. An image dataset, based on the Gaussian random reconstruction of sintered nano-Ag nanostructures, was proposed, and the equivalent thermal conductivity of sintered nano-Ag nanostructures was efficiently predicted based on a machine learning model. Image processing and model simulation were performed using MATLAB and Ansys software from scanning electron microscopy (SEM) images of sintered nano-Ag nanostructures; batch calculation of the thermal conductivity of 2D images of sintered nano-Ag nanostructures was conducted thereafter. According to the SEM image characteristics of actual sintered nano-Ag nanostructures, the images of the nanostructures at different sintering temperatures were generated by the Gaussian random model. Based on the artificial neural network (ANN) model of Bayesian optimization, the equivalent thermal conductivity corresponding to different sintered nano-Ag microstructures was accurately predicted using the microstructure image and characteristic parameters of sintered nano-Ag, with minimal loss and a high determination coefficient (0.96).

## 2. Methods

### 2.1. Effective thermal conductivity computation scheme

#### 2.1.1. Finite element model of sintered nano-Ag

Image-to-parameter automated programming can be used to improve the efficiency of analytical calculations.

In this study, image processing and modeling simulation of microstructure images were performed using MATLAB and Ansys, respectively. The results from the batch calculation of the thermal conductivity of sintered nano-Ag microstructures enhanced the understanding of the physical relationship between sintered nano-Ag microstructure and heat transfer properties.

Figure 1 displays the finite element simulation flow chart of sintered nano-Ag microstructures, utilizing image-to-parameter automated programming. Using MATLAB, the SEM image of sintered nano-Ag (Figure 2A) was analyzed and converted into a grayscale image with two-phase regions of black and white (Figure 2B). The black region corresponds to the pore, while the white region denotes the nano-Ag nanoparticles. The grayscale images were then divided into  $n$  parts equally in the  $x$  and  $y$  directions (Figure 2C) to obtain  $n \times n$  black and white pixel images. These images are stored as numerical matrices with values of 0 or 1.

After the pixel matrix was imported into Ansys, the voxel blocks were selected successively according to the coordinate position by the loop statement. The array parameters at the corresponding positions were analyzed to determine the material type of the voxel block, thereby assigning the

appropriate material properties to the current voxel block. Since sintered nano-Ag is an isotropic material, distribution in the  $x$ -,  $y$ -, and  $z$ -directions are consistent. Therefore, 2D models can be used to simulate the heat transfer behavior of sintered nano-Ag, with microstructural characteristics. A plane model of nano-Ag and air was established, where the thermal conductivity of dense nano-Ag and air is 429 and 0.03 W/mK, respectively. As the difference in thermal conductivity between dense nano-Ag and air is approximately five orders of magnitude, modeling the pore regions has minimal impact on the heat conduction simulation results. However, since isolated islands (Figure 3A) often exist in practice, omitting the air unit would require additional boundary conditions to be applied separately, increasing the workload and complicating the calculations. Hence, the pores were filled with air in this study (Figure 3B). To ensure accuracy, each pixel block was further divided into four units during the meshing process. Boundary conditions (250 and 50°C) were applied to the upper and bottom boundaries, respectively, and adiabatic boundary conditions were applied to the other boundaries. Figure 4 displays the temperature distribution density contour plot of the model (Figure 4A) and the heat flux density of each element (Figure 4B).

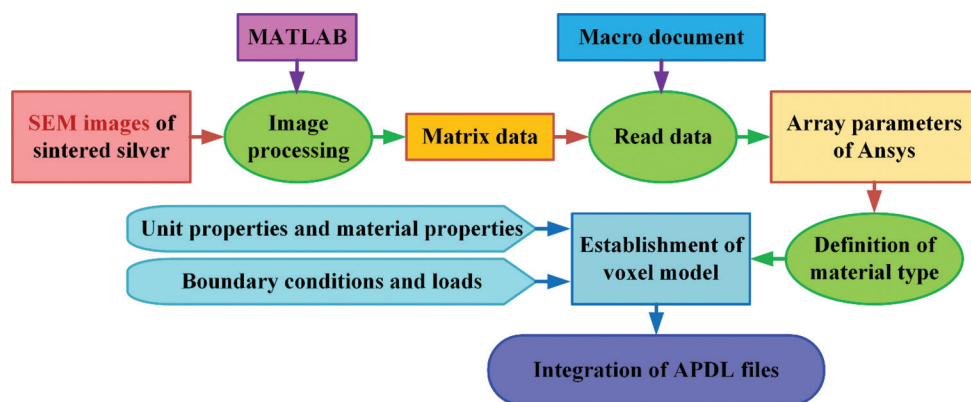


Figure 1. Finite element simulation flow chart of sintered nano-Ag microstructures  
Abbreviations: SEM: Scanning electron microscopy; APDL: ANSYS parametric design language.

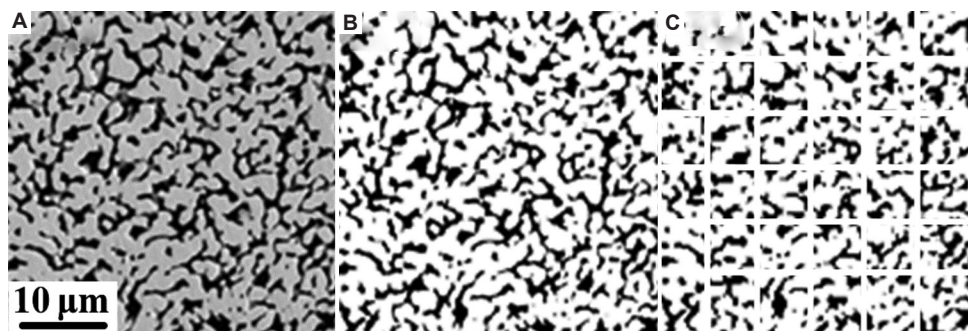
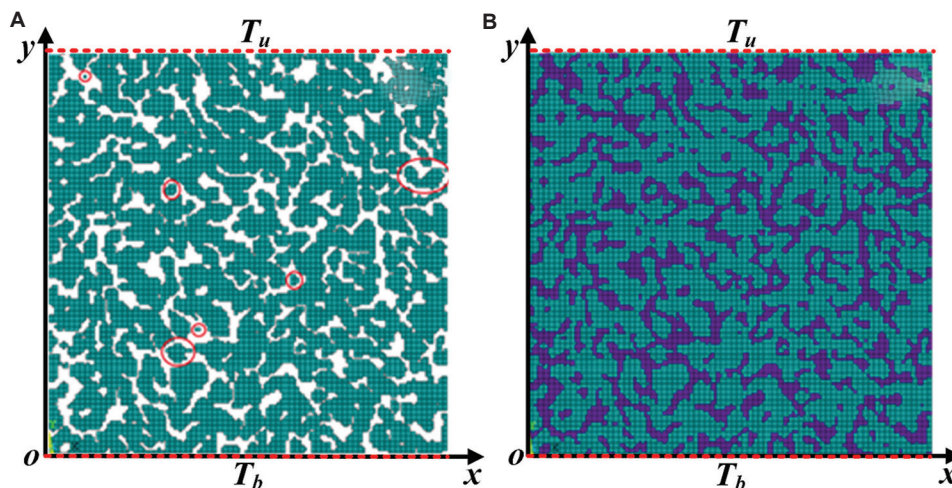


Figure 2. Gray transformation process of scanning electron microscopy (SEM) images of sintered nano-Ag: (A) SEM image of sintered nano-Ag; (B) grayscale images; and (C) image segmentation.



**Figure 3.** Comparison of microstructure finite element model before and after filling. (A) Schematic diagram of isolated islands in the model before air-filling. (B) Schematic diagram of the model after air-filling. Green boxes indicate geometric model of sintered nano Ag. Blue boxes indicate pore regions of sintered nano Ag. Red circles indicate isolated islands sintered nano Ag. Red dashed lines indicate the upper and lower boundary. Abbreviations:  $T_u$ : Upper-temperature boundary condition;  $T_b$ : Lower temperature boundary condition.

### 2.1.2. Effective thermal conductivity computation

For homogeneous materials, according to Fourier’s law of heat transfer,<sup>31</sup> the rate of heat flow in the  $y$ -direction (1D form of Fourier’s law of heat transfer) can be expressed as:

$$q_y = -k \frac{dT}{dy} \tag{I}$$

where  $q_y$  is the heat flow in the  $y$ -direction,  $k$  is thermal conductivity, and  $dT/dy$  is the temperature gradient in the  $y$ -direction.

A simple modification of Equation I yields the formula for thermal conductivity:

$$k = -\frac{q_y (y_u - y_b)}{T_u - T_b} \tag{II}$$

where  $y_u$  is the coordinate of the upper boundary in the  $y$ -direction,  $y_b$  is the coordinate of the bottom boundary in the  $y$ -direction,  $T_u$  is the temperature at the upper boundary, and  $T_b$  is the temperature of the bottom boundary.

In finite element analysis, the model is divided into units; thus, Equation II can be expressed as follows:

$$k_{eq} = -\frac{q_y (y_u - y_b) S}{(T_u - T_b) S} = -\frac{q_y (y_u - y_b) \sum_{i=1}^n S_i}{(T_u - T_b) S}$$

$$= -\frac{(y_u - y_b) \sum_{i=1}^n q_{yi} S_i}{(T_u - T_b) S} \tag{III}$$

where  $S$  is the total area of the finite element model,  $S_i$  is the area of unit  $i$ , and  $q_{yi}$  is the heat flux value of unit  $i$  in the  $y$ -direction.

Equation III is a discrete formula for calculating the equivalent thermal conductivity  $k_{eq}$ , which applies to porous media models. After determining the heat flux and area of each unit in the dense nano-Ag region in the  $y$ -direction, the equivalent thermal conductivity of the entire model can be obtained using Equation III.

In calculating the equivalent thermal conductivity of sintered nano-Ag nanoparticles using the SEM images, the number of points  $n$  must be sufficient to ensure convergence of the model results. In two SEM images obtained from the same sintering process, 18 windows of  $20 \mu\text{m}^2$  were extracted, and the number of pixels was  $50 \times 50$ ,  $100 \times 100$ ,  $150 \times 150$ , and  $200 \times 200$ . Through simulation calculation, the thermal conductivity of each window under different extraction conditions was obtained (Figure 5A and B), with the mean and range of thermal conductivity presented for each extraction condition. Notably, the difference in calculated thermal conductivity between a pixel size of  $150 \times 150$  and  $200 \times 200$  is 3.3%.

## 2.2. Machine learning method

### 2.2.1. Evaluation index of the model

To evaluate the prediction accuracy of different models, five statistical indicators were used to characterize and compare the prediction accuracy of different data-driven models.<sup>32-34</sup>

$$\text{MSE} = \frac{1}{n} \sum_{i=1}^n (y_i - y_i^*)^2 \tag{IV}$$

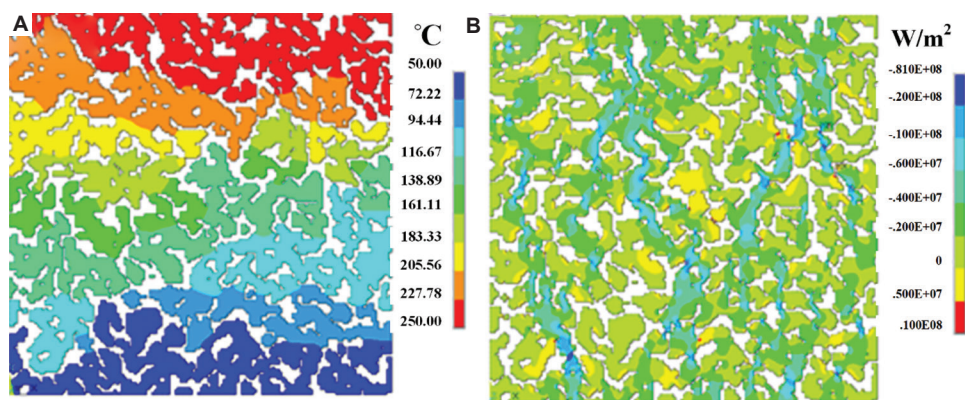


Figure 4. Finite element calculation results of the sintered nano-Ag microstructure. (A) Temperature cloud image of the model; and (B) heat flux density of each element in the  $y$ -direction.

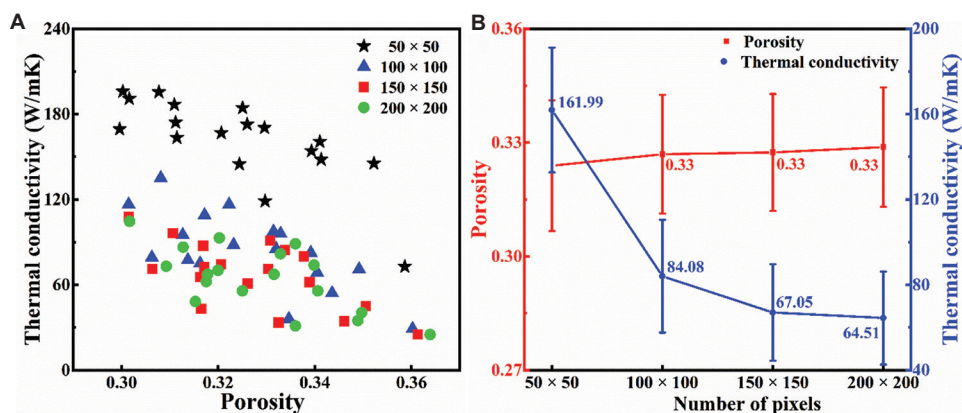


Figure 5. Finite element calculation results of models with different precision. (A) Thermal conductivity distribution of models corresponding to different porosity; and (B) the mean value and range of thermal conductivity under each extraction condition.

$$R^2 = 1 - \frac{\sum_{i=1}^n (y_i - y_i^*)^2}{\sum_{i=1}^n (y_i - \bar{y})^2} \quad (V)$$

Where  $y_i$  and  $y_i^*$  are the  $i$ -th actual output value and predicted output value, respectively;  $\bar{y}$  and  $\bar{y}^*$  are the average actual output value and the average predicted output value, respectively; and  $n$  is the number of samples. The mean squared error (MSE), as displayed in Equation IV, is an indicator used to measure the average squared difference between model predictions and actual observations. MSE is commonly used as the loss function to estimate the inconsistency between predicted values and actual values.<sup>32</sup> The coefficient of determination  $R^2$ , as displayed in Equation V, represents the determination coefficient, indicating the degree of fit between the regression model and actual data.<sup>33,34</sup> When  $R^2$  is close to 1, it indicates that the model fits the actual data well.

### 2.2.2. Data preparation and network selection

A large amount of high-quality microstructure data of sintered nano-Ag is required to simulate the

microstructural effect on the thermal conductivity of sintered nano-Ag. After an open operation and convolution kernel size adjustment, random images of crystal nucleus distribution generated by the Gaussian random model were used to simulate the growth process of a crystal nucleus (Figure 6). Finally, 186 images of sintered nano-Ag microstructure, corresponding to three different pixel sizes and sintering times, were obtained. Based on the images, a plane model of the microstructure was built in Ansys to calculate the thermal conductivity of the model in the  $x$ - and  $y$ -directions, while the boundary conditions (i.e., sintering temperatures) were applied to the upper and bottom boundaries. From a microstructural perspective, the input formats of neural network calculations can be divided into two categories: (i) One method involves extracting the index parameters of the microstructure as numerical inputs, and (ii) the other method directly uses microstructure images of sintered nano-Ag as input. The former provides better computational speed but offers limited information about the model; the latter enables more comprehensive and accurate feature extraction but

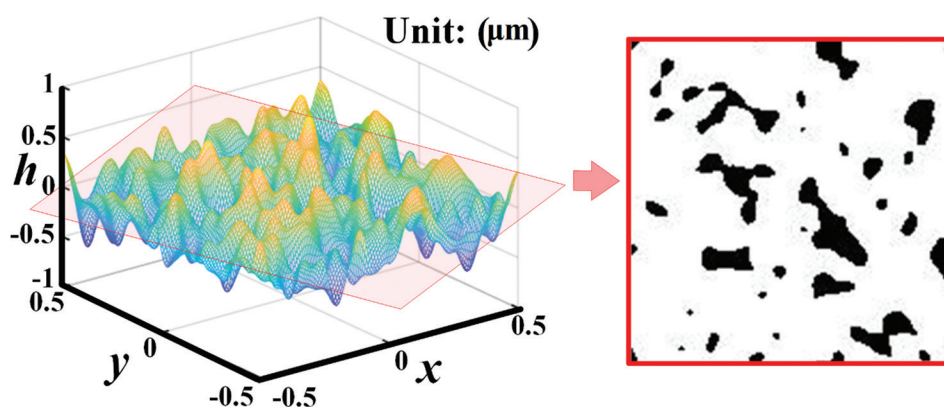


Figure 6. A 2D grayscale image of pores generated based on the 3D Gaussian random model. Note: x, y and h are the axes of the 3D Gaussian model, corresponding to the length, width, and height, respectively

requires more training data and time, making it harder to train. Given the advantages and disadvantages of both numerical features and image input types in the calculation of neural network models, numerical and image datasets of the model were established in this study to obtain more comprehensive information without affecting the calculation speed.

The characteristic parameters of the sintered nano-Ag SEM images were extracted by ImageJ, including average particle size, particle circumference, and porosity, to form a dataset of numerical input. Since the three characteristic parameters extracted are not directional – remaining unchanged regardless of image inversion or rotation – the simulated thermal conductivity in the x- and y-directions is averaged in the output dataset to obtain the average thermal conductivity as the output of the numerical input model. To fully utilize the 186 sintered nano-Ag microstructure images, the dataset was augmented by flipping each image left and right, flipping it up and down, and rotating it 180°, resulting in three additional images for each original. In other words, the original dataset can be quadrupled, resulting in a total of 744 datasets without additional simulation time. This approach enhances the amount of data used for model training and further improves model accuracy. Notably, the thermal conductivity of the microstructure model based on these three images is the same as that of the original image in the x- and y-directions. The numerical and corresponding image data serve as inputs, while the simulated thermal conductivity in the x- and y-directions is the output of the model when establishing the corresponding dataset. This process occurs simultaneously with the training of neural networks. Using the bootstrap method, the numerical and image datasets are divided into a training set and a testing set in a 7:3 ratio for model training.

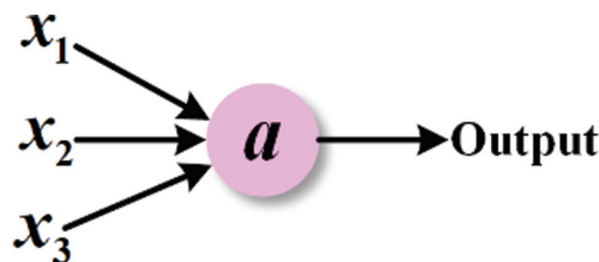


Figure 7. Perceptron structure diagram

### 2.2.3. Principles and hyperparameter tuning of machine learning models

The ANN consists of multiple fully connected layers, i.e., each neuron is connected to all the neurons in the previous layer.<sup>35</sup> In ANN, a simple model with several inputs and one output is called the perceptron, i.e., from the perspective of a single neuron locally (Figure 7). The perceptron consists of a linear relation and an activation function  $\sigma(z)$ . The output formula for the single perceptron can be expressed as:

$$a = \sigma(z) = \sigma\left(\sum_{i=1}^n \omega_i x_i + b\right) \tag{VI}$$

The lines between each neuron in ANN represent a weight coefficient  $w$ , with each neuron corresponding to a bias  $b$ . In addition, to satisfy the non-linear relationship between input and output, the activation function  $\sigma$  is added. Common activation functions include ReLU, Sigmoid, and Tanh. The ReLU activation function is selected for this study. As a common activation function, ReLU helps avoid the gradient disappearance problem by introducing non-linear transformation and sparse activation. This effectively increases the expressive power of the neural network, making the model more distinguishable. The specific formula of ReLU is expressed as follows:

$$\text{ReLU: } f(x) = \begin{cases} x & \text{if } x > 0 \\ \theta x & \text{if } x \leq 0 \end{cases} \quad (\text{VII})$$

An ANN with more hidden layers and neurons is typically regarded as a deep neural network (DNN). As displayed in Figure 8, ANN is the result of multiple perceptrons in parallel and in series.<sup>36</sup> The network features three hidden layers, and the number of neurons in each hidden layer is denoted as  $i, j$ , and  $k$ , respectively. The output formula of the ANN network composed of neurons in  $n$  layers is expressed as follows:

$$a_i^l = \sigma(z_i^l) = \sigma\left(\sum_{j=1}^n \omega_{ij}^l a_j^{l-1} + b_i^l\right) \quad (\text{VIII})$$

where  $a_i^l$  represents the  $i$ -th neuron of layer  $l$  in ANN;  $w_{ij}^l$  represents the weight coefficient from the  $j$ -th neuron of layer  $l-1$  to the  $i$ -th neuron of layer  $l$ ; and  $b_i^l$  represents the offset corresponding to the  $i$ -th neuron in the  $l$  layer. When expressed in matrix form, the formula can be simplified as:

$$a^l = \sigma(z^l) = \sigma(W^l a^{l-1} + b^l) \quad (\text{IX})$$

The main computation process of neural networks involves forward propagation and backpropagation. The forward propagation algorithm uses several weight coefficient matrices  $W$  and bias vector  $b$  to perform a series of linear operations and activation operations with input vector  $x$ . From the input layer, the output of the previous layer is used to calculate the output of the next layer until the result of the final output layer is obtained. Backpropagation uses forward propagation to calculate the output of the training sample, with the loss function measuring the difference between the predicted and actual values. A typical backpropagation algorithm (BP) minimizes the loss function through iterative optimization using the gradient descent method to identify the appropriate linear coefficient matrix  $W$  and bias vector  $b$  for the hidden and output layers. The output calculated

from the training samples should be equal to or close to the target value. The loss function is calculated as follows:

$$J(W, b, x, y) = \frac{1}{2} \|a^l - y\|_2^2 = \frac{1}{2} \|\sigma(W^l a^{l-1} + b^l) - y\|_2^2 \quad (\text{X})$$

Where  $a^l$  is the predicted value of the output layer, and  $y$  is the target value of the output.

During model training, the most widely accepted Adam optimizer was selected. The performance and generalization of the model were evaluated using the MSE of the testing set. Subsequently, the hyperparameters of the neural network are tuned based on the MSE value to improve the performance and stability of the model. Grid search is the most widely used hyperparameter search algorithm, which determines the optimal value by searching all the points within the search range.<sup>37</sup> Generally, given a large search range and a small step size, the grid search method can identify the global maximum or minimum value, but it heavily consumes computing resources.

In contrast, a random search does not analyze all parameter values but samples a fixed number of parameters from a specified distribution. Random search can also be used to identify a global optimal solution if the set of random sample points is large enough. Compared with the grid search method, the random search method is faster, but its accuracy cannot be guaranteed. Bayesian optimization, an effective global optimization algorithm, was proposed by Snoek *et al.*<sup>38</sup> to be used for parameter tuning in machine learning. Its concept involves updating the posterior distribution of the objective function by continuously adding sample points through the Gaussian process until the posterior distribution closely approximates the true distribution. In short, it accounts for the last sampling point to better adjust the current sampling point, maximize the benefit of the next sampling point, and avoid unnecessary sampling to the greatest extent. Compared with other methods,

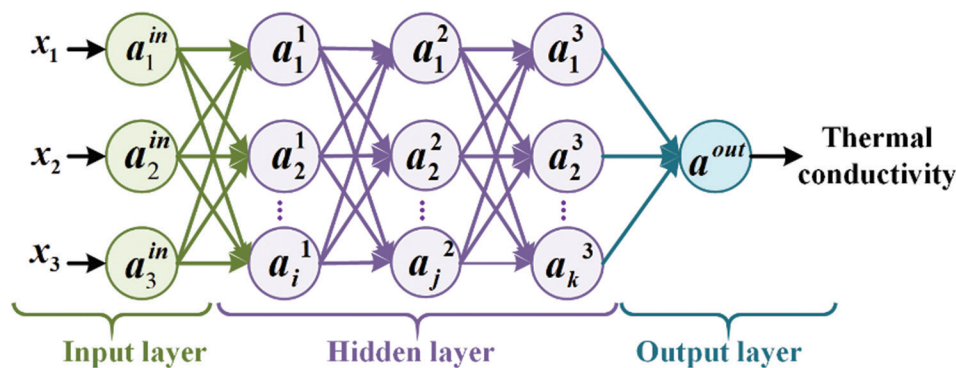


Figure 8. Artificial neural network structure diagram

Bayesian optimization has been widely recognized for its convenience and accuracy.

Bayesian optimization is derived from the famous “Bayes theorem”:<sup>39</sup>

$$p(f|D) = \frac{p(D|f)p(f)}{p(D)} \quad (XI)$$

where  $f$ ,  $D = \{(x_1, y_1), (x_2, y_2), \dots, (x_n, y_n)\}$ ,  $x_n$ , and  $y_n$  represent the unknown objective function, the set of observed sampling points, the decision vector, and the observed value of the sampling point, respectively;  $p(D|f)$  and  $p(f)$  represents the likelihood distribution of  $y$  and the prior probability distribution of  $f$  (that is, the assumption about the unknown objective function state); and  $p(D)$  represents the marginal likelihood distribution of  $f$ . The function  $p(D)$  is usually difficult to calculate because it involves the product and integral of the probability density function. However, since it does not depend on  $f$ , it is treated as a normalized constant in Bayesian optimization. In addition,  $p(f|D)$  represents the posterior probability distribution of  $f$ , which describes the confidence of the unknown objective function after modifying the prior function from the observed data set.

The Bayesian optimization algorithm consists of two core parts: the probabilistic agent model and the acquisition function. The probabilistic agent model includes the prior probability model and the observation model. The former is  $p(f)$ , while the latter describes the mechanism by which the observed data are generated, the likelihood distribution  $p(D|f)$ . The posterior probability distribution  $p(f|D)$ , containing the observations of the latest evaluation points, is obtained using the Bayesian formula to update the probabilistic agent model. According to the posterior probability distribution, the next most “potential” evaluation point is selected by maximizing the collection function, and an effective collection function can ensure that the selected evaluation point sequence minimizes the total loss value:

$$Loss = \sum_{i=1}^n |y^* - y_i| \quad (XII)$$

where  $y^*$  represents the optimal solution of the current evaluation point.

The specific calculation process of the Bayesian optimization algorithm involves an iterative process of parameter updates, and its specific algorithm framework is presented in Table 1.<sup>40</sup>

Figure 9 displays the principle of the Bayesian optimization algorithm. Each repeat sampling generates a minimum value for the objective function. After the first random sampling of the function, the second sampling

Table 1. Bayesian optimization algorithm calculation process

Bayesian optimization algorithm
For $n=1, 2, \dots$ , do
a. Obtain the next evaluation point $x_{n+1}$ by maximizing the acquisition function $\alpha$
b. Get the objective function value of the evaluation point $y_{n+1}$ ;
c. Augment data $D_{n+1} = \{D_n, (x_{n+1}, y_{n+1})\}$ ;
d. Update probabilistic proxy model end for

assesses points near the possible minimum value and in regions that have not been sampled. This approach helps avoid entrapment in the local optima, improves proxy function approximation of the true objective function, and facilitates finding the minimum value of the objective function. In simple terms, the Bayesian optimization algorithm selects the next sampling point to maximize the return.

For the tuning method, the type and range of tuning parameters need to be defined. In the ANN model, the learning rate, number of hidden layers, and number of neurons in each layer are selected as the tuning parameters. Among them, the learning rate in the optimizer is an important hyperparameter in the neural network, regulating the step size of each parameter update and directly affecting the convergence speed and performance of the model. The number of hidden layers and neurons in each layer determines the structure of the model. To streamline parameter adjustment, the number of neurons in each layer is set to be the same to ensure that the number of hidden layers and neurons in each layer can be used as two independent parameters for parameter adjustment.

Figure 10 presents the results of Bayesian optimization of hyperparameters in the ANN model. The learning rate ranges from  $1e^{-4}$  to 0.1 and is distributed exponentially to improve optimization efficiency. The number of hidden layers is presented as an integer, ranging from 1 to 5, while the number of neurons is presented as an integer, ranging from 1 to 140. The evaluation index MSE (Equation IV) of the model is reflected by the color of the data points, and the corresponding value range is referred to the color scale on the right. Sampling occurs across the entire hyperparameter space, avoiding the local optima. The points around the final optimal result are relatively dense, indicating that the model undergoes fine-tuning and optimization at the later stages. The final hyperparameters include two hidden layers, each with 32 neurons, and a learning rate of  $9.29e^{-4}$ .

### 3. Results and discussion

The established ANN model was used to map the relationship between the input characteristics

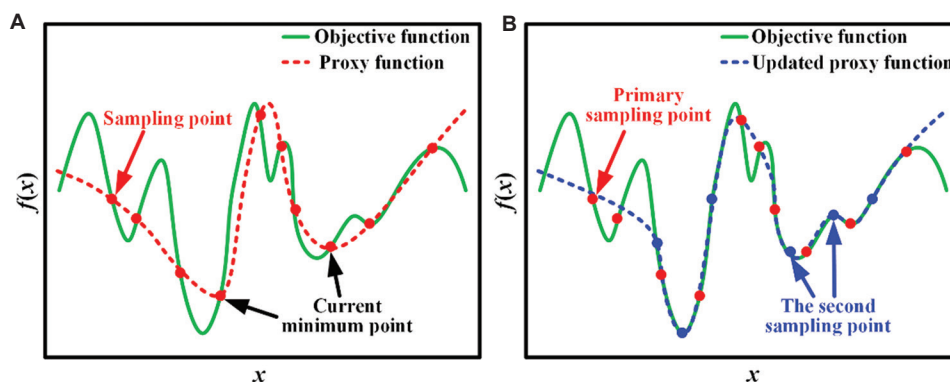


Figure 9. Principle of the Bayesian optimization algorithm. Results of the (A) first sampling and (B) second sampling.

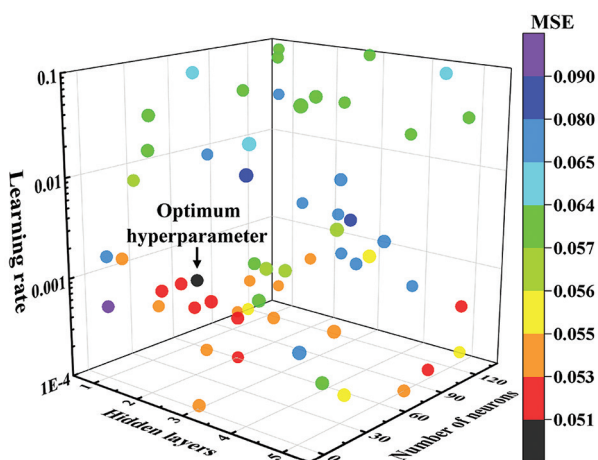


Figure 10. Hyperparameter Bayesian optimization results of the artificial neural network  
Abbreviation: MSE: Mean square error.

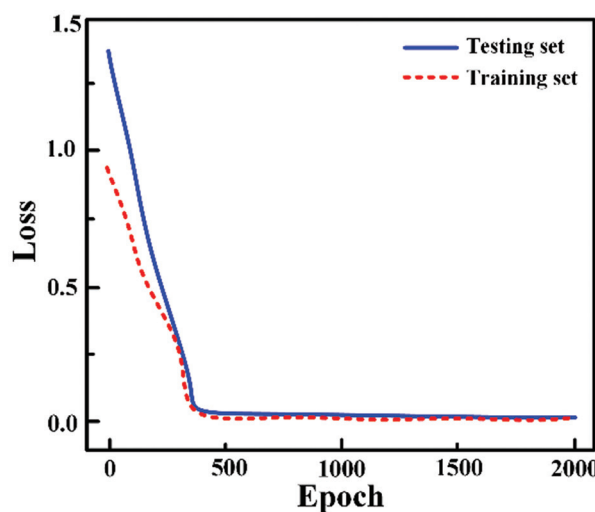


Figure 11. Loss curve of the artificial neural network

(microstructure characteristics of sintered nano-Ag) and the output value (thermal conductivity of sintered nano-Ag). According to the loss function defined by Equation XII, after 2000 training of the epoch, the training loss and testing loss decreased over time. All losses converge at about 400 cycles, dropping below 0.05, and remain stable in the subsequent training cycles (Figure 11). The results indicate that the 500 epochs reflect the actual training effect of ANN, without overfitting in the thermal conductivity prediction of sintered nano-Ag.

In addition to the MSE, the determination coefficient ( $R^2$ ) was also used to evaluate the performance of the ANN model. The coefficient  $R^2$  is defined by Equation V. A higher  $R^2$  value indicates that the model has better prediction ability for the target parameters. Figure 12 displays the comparison between the predicted and actual thermal conductivity of sintered nano-Ag. As observed, the distribution of data points (blue dots) is focused around the

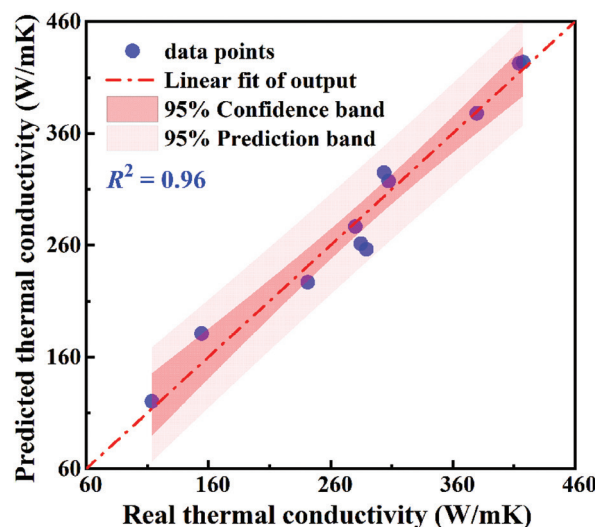


Figure 12. The predicting performance of thermal conductivity testing

ideal prediction trendline (red dashed line), indicating that the predicted parameters are relatively close to the actual parameters. The value of  $R^2$  is as high as 0.96, indicating that the ANN model based on Bayesian optimization has a good predictive ability for the correlation analysis between microstructure characteristics and thermal conductivity of sintered nano-Ag. The 95% confidence region also confirms that the proposed optimal ANN model has good predictive performance. The confidence interval represents the knowledge level of the best fitting line and determines that the true linear fitting output is within the interval. In Figure 12, when the trained ANN model was used to predict thermal conductivity, the confidence interval between the predicted output and the real output was compared; it was found that most of the predicted points overlapped with the actual value, with smaller differences corresponding to higher prediction accuracy.

The factors that affect the thermal properties of sintered nano-Ag, such as sintering process parameters, affect the microstructure of sintered Ag nanoparticles. However, in existing studies, microstructure parameters are rarely used in thermal conductivity models.<sup>30</sup> Notably, our study utilized the microscopic reconstruction method, which combines Gaussian random reconstruction and finite element, effectively studying the thermal conductivity changes as the microstructure changes under the influence of sintering parameters. However, due to limitations in the dataset and the difficulty of obtaining it, we only analyzed the evolution of microscopic grains at different sintering times using the open operation method, without considering the effect of sintering temperature. Nevertheless, if the influence of sintering temperature changes on thermal conductivity is included, the model would remain valid. Rong *et al.*<sup>29</sup> mentioned in their study that features selected from a large descriptor space may limit the predictive accuracy of machine learning models. It is worth noting that we simultaneously used both the image dataset and the feature parameter dataset for training, effectively mitigating this issue and enhancing the model's generalization ability for different types of structures. We are working to integrate the aforementioned factors to study the microstructure evolution of sintered nano-Ag, aiming to obtain a more comprehensive dataset that captures the changes in thermal characteristics with respect to microstructure parameters.

## 4. Conclusion

We presented the image of sintered nano-Ag microstructure based on Gaussian reconstruction, where feature parameters and image data are separately extracted to form a dataset. The equivalent thermal conductivity of sintered nano-Ag is then predicted using a machine-learning model. In summary, our key findings are as follows:

- (i). Image processing and modeling simulation methods for SEM images of sintered nano-Ag microstructure were established by MATLAB and Ansys software. Batch calculation of the thermal conductivity from 2D images of sintered nano-Ag microstructure was performed accordingly. Based on the SEM image characteristics of actual sintered nano-Ag microstructure, 186 images of the microstructure, obtained from using 3-pixel sizes and different sintering times, were reconstructed using the Gaussian random model. The thermal conductivity in the  $x$ - and  $y$ -directions of the microstructure plane model was obtained by finite element simulation.
- (ii). Given the advantages and disadvantages of both the numerical parameters and the image input types for neural network analysis, the numerical dataset and the image dataset are established, respectively. An image was obtained from the reconstructed model of the sintered nano-Ag microstructure, and the dataset was enhanced four times. The model accuracy can be further improved by enhancing the amount of data used for model training.
- (iii). Based on the Bayesian optimized ANN model, the average particle size, circumference, and porosity were taken as input parameters to predict the equivalent thermal conductivity of sintered nano-Ag. The final determination coefficient of the ANN model for the equivalent thermal conductivity prediction is 0.96. The results are of great significance for evaluating the microstructure and physical properties of sintered nano-Ag. Hence, future studies should focus on the physical mechanisms based on existing models.

## Acknowledgments

The authors would like to express their gratitude for the support from the National Natural Science Foundation of China (No. 12272012) and acknowledge the AI tool SparkDesk (iFLYTEK) for enhancing the language quality and readability of the manuscript.

## Funding

This research was financially supported by the National Natural Science Foundation of China (No. 12272012).

## Conflict of interest

The authors declare that they have no known competing financial interests or personal relationships that could have appeared to influence the work reported in this paper.

## Author contributions

*Conceptualization:* Jiahui Wei, Yanwei Dai  
*Formal analysis:* Libo Zhao, Jiahui Wei

*Investigation:* Jiahui Wei, Daowei Wu, Yuting Zhang, Kui Li, Fei Qin

*Methodology:* Yanwei Dai, Libo Zhao, Jiahui Wei

*Writing – original draft:* Libo Zhao, Jiahui Wei, Yanwei Dai

*Writing – review & editing:* Libo Zhao, Yanwei Dai, Jiahui Wei

## Ethics approval and consent to participate

Not applicable.

## Consent for publication

Not applicable.

## Availability of data

The data presented in this study are available upon request from the corresponding author due to data protection.

## References

- Herboth T, Guenther M, Fix A, Wilde J. Failure Mechanisms of Sintered Silver Interconnections for Power Electronic Applications. In: *IEEE 63<sup>rd</sup> Electronic Components and Technology Conference*. Las Vegas, NV, USA; 2013. p. 1621-1627.  
doi: 10.1109/ECTC.2013.6575789
- Ordenez-Miranda J, Hermens M, Nikitin I, Kouznetsova VG, van der Sluis O, Ras MA, Volz S. Measurement and modeling of the effective thermal conductivity of sintered silver pastes. *Int J Therm Sci*. 2016;108:185-194.  
doi: 10.1016/j.ijthermalsci.2016.05.014
- Signor L, Kumar P, Tressou B, *et al.* Evolution of the thermal conductivity of Sintered silver joints with their porosity predicted by the finite element analysis of real 3D microstructures. *J Electron Mater*. 2018;47:4170-4176.  
doi: 10.1007/s11664-018-6253-2.
- Sghuri A, Billaud Y, Signor L, Saury D, Milhet X. Experimental investigation of thermal conductivity during aging of nanoporous sintered silver. *Acta Mater*. 2023;257:119109.  
doi: 10.1016/j.actamat.2023.119109
- Hu X, Martin HA, Poelma R, *et al.* Exploring the process-microstructure-thermal properties relationship of resin-reinforced Ag sintering material for high-power applications via 3D FIB-SEM nanotomography. *Mater Des*. 2024;244:113185.  
doi: 10.1016/j.matdes.2024.113185
- Zhao Z, Zhang H, Zou G, *et al.* A predictive model for thermal conductivity of nano-Ag sintered interconnect for a SiC die. *J Electron Mater*. 2019;48:2811-2825.  
doi: 10.1007/s11664-019-06984-3
- Qin F, Hu Y, Dai Y, An T, Chen P. Evaluation of thermal conductivity for sintered silver considering aging effect with microstructure based model. *Microelectron Reliab*. 2020;108:113633.  
doi: 10.1016/j.microrel.2020.113633
- Qin F, Hu Y, Dai Y, *et al.* Crack effect on the equivalent thermal conductivity of porously sintered silver. *J Electron Mater*. 2020;49:5994-6008.  
doi: 10.1007/s11664-020-08325-1
- Qin F, Zhao S, Dai Y, Hu Y, An T, Gong Y. Mud-cracking effect of sintered silver layer on quantifying heat transfer behavior of SiC devices under power cycling: Voronoi tessellation model. *IEEE Trans Compon Packag Manuf Technol*. 2022;12(6):964-972.  
doi: 10.1109/TCPMT.2022.3178226
- Kim YJ, Park BH, Hyun SK, Nishikawa H. The influence of porosity and pore shape on the thermal conductivity of silver sintered joint for die attach. *Mater Today Commun*. 2021;29:102772.  
doi: 10.1016/j.mtcomm.2021.102772
- Chen H, Du Z, Li X, Zhou H, Liu Z. Identification of pipe inner surface in heat conduction problems by deep learning and effective thermal conductivity transform. *Eng Comput*. 2020;37(9):3505-3523.  
doi: 10.1108/EC-01-2020-0012
- Huang Q, Hong D, Niu B, Long D, Zhang Y. An interpretable deep learning strategy for effective thermal conductivity prediction of porous materials. *Int J Heat Mass Transfer*. 2024;221:125064.  
doi: 10.1016/j.ijheatmasstransfer.2023.125064
- Qin G, Wei Y, Yu L, *et al.* Predicting lattice thermal conductivity from fundamental material properties using machine learning techniques. *J Mater Chem A*. 2023;11(11):5801-5810.  
doi: 10.1039/D2TA08721A
- Li RY, Lee E, Luo TF. A unified deep neural network potential capable of predicting thermal conductivity of silicon in different phases. *Mater Today Phys*. 2020;12:100181.  
doi: 10.1016/j.mtphys.2020.100181
- Yang ZH, Wu XX, He XD, Guan XF. A multiscale analysis-assisted two-stage reduced-order deep learning approach for effective thermal conductivity of arbitrary contrast heterogeneous materials. *Eng Appl Artif Intell*. 2024;136:108916.  
doi: 10.1016/j.engappai.2024.108916
- Kim TH, Park JH, Jung KW, Kim J, Lee EH. Application of convolutional neural network to predict anisotropic

- effective thermal conductivity of semiconductor package. *IEEE Access*. 2022;10:51995-52007.  
doi: 10.1109/ACCESS.2022.3174882
17. Du CJ, Zou GS, Zhanwen A, *et al*. Highly accurate and efficient prediction of effective thermal conductivity of sintered silver based on deep learning method. *Int J Heat Mass Transfer*. 2023;201:123654.  
doi: 10.1016/j.ijheatmasstransfer.2022.123654
  18. Du CJ, Zou G, Feng B, *et al*. Predicting effective thermal conductivity of sintered silver by microstructural-simulation-based machine learning. *J Electron Mater*. 2023;52(4):2347-2358.  
doi: 10.1007/s11664-022-10172-1
  19. Long X, Mao MH, Su TX, Su YT, Tian MK. Machine learning method to predict dynamic compressive response of concrete-like material at high strain rates, *Def Technol*. 2023;23:100-111.  
doi: 10.1016/j.dt.2022.02.003
  20. Mao M, Wang W, Lu C, Jia F, Long X. Machine learning for board-level drop response of BGA packaging structure. *Microelectron Reliab*. 2022;134:114553.  
doi: 10.1016/j.microrel. 2022.114553
  21. Sezer A, Altan A. Detection of solder paste defects with an optimization-based deep learning model using image processing techniques. *Soldering Surf Mount Technol*. 2021;33(5):291-298.  
doi: 10.1108/SSMT-04-2021-0013
  22. Long X, Lu CH, Su YT, Dai YH. Machine learning framework for predicting the low cycle fatigue life of lead-free solders. *Eng Failure Anal*. 2023;148:107228.  
doi: 10.1016/j.engfailanal.2023.107228
  23. Prisacaru A, Gromala P, Han B, Zhang GQ. Degradation estimation and prediction of electronic packages using data-driven approach. *IEEE Trans Ind Electron*. 2021;69(3):2996-3006.  
doi: 10.1109/TIE.2021.3068681
  24. Samavatian V, Fotuhi-Firuzabad M, Samavatian M, Dehghanian P, Blaabjerg F. Iterative machine learning-aided framework bridges between fatigue and creep damages in solder interconnections. *IEEE Trans Compon Packag Manuf Technol*. 2021;12(2):349-358.  
doi: 10.1109/TCPMT.2021.3136751
  25. Long X, Lu CH, Shen ZY, Su YT. Identification of mechanical properties of thin-film elastoplastic materials by machine learning. *Acta Mech Sol Sin*. 2023;36:13-21.  
doi: 10.1007/s10338-022-00340-5
  26. Kuo HC, Chang CY, Yuan C, Chiang KN. Wafer-level packaging solder joint reliability lifecycle prediction using SVR-based machine learning algorithm. *J Mech*. 2023;39:183-190.  
doi: 10.1093/jom/ufad016
  27. Samavatian V, Fotuhi-Firuzabad M, Samavatian M, Dehghanian P, Blaabjerg F. Correlation-driven machine learning for accelerated reliability assessment of solder joints in electronics. *Sci Rep*. 2020;10(1):14821.  
doi: 10.1038/s41598-020-71926-7
  28. Wei H, Zhao SS, Rong QY, Bao H. Predicting the effective thermal conductivities of composite materials and porous media by machine learning methods. *Int J Heat Mass Transfer*. 2018;127:908-916.  
doi: 10.1016/j.ijheatmasstransfer.2018.08.082
  29. Rong QY, Wei H, Huang XY, Bao H. Predicting the effective thermal conductivity of composites from cross sections images using deep learning methods. *Compos Sci Technol*. 2019;184:107861.  
doi: 10.1016/j.compscitech.2019.107861
  30. Fei W, Narsilio GA, Disfani MM. Predicting effective thermal conductivity in sands using an artificial neural network with multiscale microstructural parameters. *Int J Heat Mass Transfer*. 2021;170:120997.  
doi: 10.1016/j.ijheatmasstransfer.2021.120997
  31. Carslaw HS, Jaeger JC. *Conduction of Heat in Solids*. London: Clarendon Press; 1992.  
doi: 10.1007/978-1-4939-2565-0\_2
  32. Märtens M, Izzo D, Krzic A, Krzic A, Cox D. Super-resolution of PROBA-V images using convolutional neural networks. *Astrodynamics*. 2019;3:387-402.  
doi: 10.1007/s42064-019-0059-8
  33. Manan A, Zhang P, Ahmad S, Ahmad J. Optimizing hybrid fibre-reinforced polymer bars design: A machine learning approach. *J Polym Mater*. 2024;41(1):15-44.  
doi: 10.32604/jpm.2024.053859
  34. Suryawanshi A, Behera N. Application of machine learning for prediction dental material wear. *J Polym Mater*. 2023;40(3-4):305-316.  
doi: 10.32381/JPM.2023.40.3-4.11
  35. Krishnamoorthy K, Prabhu N. Tensile failure characterization of glass/epoxy composites using acoustic emission RMS data. *J Polym Mater*. 2023;40(3-4):215-226.  
doi: 10.32381/JPM.2023.40.3-4.7
  36. Peng H, Bai X. Comparative evaluation of three machine learning algorithms on improving orbit prediction accuracy. *Astrodynamics*. 2019;3(4):325-343.  
doi: 10.1007/s42064-018-0055-4
  37. Li WB, Song Y, Cheng L, Gong SP. Closed-loop deep neural

- network optimal control algorithm and error analysis for powered landing under uncertainties. *Astrodynamics*. 2023;7(2):211-228.  
doi: 10.1007/s42064-022-0153-1
38. Snoek J, Larochelle H, Adams RP. Practical bayesian optimization of machine learning algorithms. *Adv Neural Inf Process Syst*. 2012;25:2951-2959.  
doi: 10.5555/2999325.2999464
39. Kaiser J, Xu CR, Eichler A, *et al*. Reinforcement learning-trained optimisers and bayesian optimisation for online particle accelerator tuning. *Sci Rep*. 2024;14(1):15733.  
doi: 10.1038/s41598-024-66263-y
40. Shahriari B, Swersky K, Wang ZY, Adams RP, Freitas N. Taking the human out of the loop: A review of bayesian optimization. *Proc IEEE*. 2015;104(1):148-175.  
doi: 10.1109/JPROC. 2015.2494218